

Supernova 2014J at M82: II. Direct Analysis of Spectra Obtained with Isaac Newton and William Herschel Telescopes

Patrick Vallely¹, M.E. Moreno-Raya², E. Baron^{1,3}, Pilar Ruiz-Lapuente^{4,5}, I. Domínguez⁶, Lluís Galbany^{7,8}, J. I. González Hernández^{9,10}, J. Méndez¹¹, M. Hamuy^{8,7}, A. R. López-Sánchez^{12,13}, S. Catalán¹⁴, E. Cooke¹⁵, C. Fariña¹¹, R. Génova-Santos^{9,10}, R. Karjalainen¹¹, H. Lietzen^{9,10}, J. McCormac¹⁴, F. Riddick¹¹, J. A. Rubiño-Martín^{9,10}, I. Skillen⁵, V. Tudor¹¹, O. Vaduvescu¹¹

¹Homer L. Dodge Department of Physics and Astronomy, University of Oklahoma, 440 W. Brooks, Rm 100, Norman, OK, 73019-2061 USA

²Departamento de Investigación Básica, CIEMAT, Avda. Complutense 40, 28040, Madrid, Spain

³Hamburger Sternwarte, Gojenbergsweg 112, 21029 Hamburg, Germany

⁴Instituto de Física Fundamental, Consejo Superior de Investigaciones Científicas, c/. Serrano 121, E-28006, Madrid, Spain

⁵Institut de Ciències del Cosmos (UB-IEEC), c/. Martí i Franqués 1, E-08028, Barcelona, Spain

⁶Universidad de Granada, E-18071, Granada, Spain

⁷Millennium Institute of Astrophysics, Universidad de Chile, Chile

⁸Departamento de Astronomía, Universidad de Chile, Santiago, Chile

⁹Instituto de Astrofísica de Canarias, 38200 La Laguna, Tenerife, Spain

¹⁰Departamento de Astrofísica, Universidad de La Laguna (ULL), 38206 La Laguna, Tenerife, Spain

¹¹Isaac Newton Group of Telescopes, Apto. 321, E-38700 Santa Cruz de la Palma, Canary Islands, Spain

¹²Australian Astronomical Observatory, PO BOX 296, Epping, NSW 1710, Australia

¹³Department of Physics and Astronomy, Macquarie University, NSW 2109, Australia

¹⁴Department of Physics, University of Warwick, Coventry CV47AL, UK

¹⁵School of Physics and Astronomy, University of Nottingham, University Park, Nottingham, NG7 2RD, UK

Accepted xxx Received xx; in original form xxx

ABSTRACT

We analyze a time series of optical spectra of SN 2014J from almost two weeks prior to maximum to nearly four months after maximum. We perform our analysis using the SYNOW code, which is well suited to track the distribution of the ions with velocity in the ejecta. We show that almost all of the spectral features during the entire epoch can be identified with permitted transitions of the common ions found in normal SNe Ia in agreement with previous studies.

We show that 2014J is a relatively normal SN Ia. At early times the spectral features are dominated by Si II, S II, Mg II, and Ca II. These ions persist to maximum light with the appearance of Na I and Mg I. At later times iron-group elements also appear, as expected in the stratified abundance model of the formation of normal type Ia SNe.

We do not find significant spectroscopic evidence for oxygen, until 100 days after maximum light, which also indicates that there is not significant mixing of ⁵⁶Ni to higher velocities. The +100 day identification of oxygen is tentative, and would imply significant mixing of unburned or only slight processed elements down to a velocity of 6,000 km s⁻¹. Our results are in relatively good agreement with other analyses in the IR. We briefly compare SN 2011fe to SN 2014J and conclude that the differences could be due to different central densities at ignition or differences in the C/O ratio of the progenitors.

1 INTRODUCTION

SN 2014J, located in M82 only a 3.3 Mpc away (Foley et al. 2014), is the closest SN Ia observed in the last 40 years. As

the nearest modern SNe Ia, SN 2014J has been extremely well observed: in γ -rays (Diehl et al. 2014; Churazov et al. 2014), X-rays (Margutti et al. 2014), by HST (Foley et al.

2014; Kelly et al. 2014), optical (Goobar et al. 2014; Nielsen et al. 2014; Amanullah et al. 2014; Ashall et al. 2014) at high resolution (Welty et al. 2014; Ritchey et al. 2015; Jack, Baron & Hauschildt 2015; Graham et al. 2015), near-IR (Marion et al. 2015; Friesen et al. 2014), mid-IR (Johansson et al. 2015; Telesco et al. 2015), polarimetry (Kawabata et al. 2014), with rapid photometry (Siverd et al. 2015), and in radio (Pérez-Torres et al. 2014).

In Galbany et al. (2015) (henceforth Paper I) we present a long time baseline set of optical spectroscopy and we analyzed the dataset using wavelength coincidences to obtain line identifications and velocities. Here we take that analysis one step further using the parameterized synthetic-spectrum code SYNOW. In the SYNOW framework, we fit the observed spectra, identify the line features, and determine the photospheric velocity and the velocity extent of the ions of SN 2014J at each epoch.

SYNOW is a parameterized line scattering code that includes the effects for multiple scattering. An opaque photosphere illuminates the atmosphere with a blackbody. The velocity is homologous, $v \propto r$, and the photosphere is at a velocity coordinate v_{ph} . The source function is taken to be that of resonance scattering $S = W(r)I_{\text{ph}}$, where I_{ph} is the intensity from the photosphere and

$$W = \frac{1}{2} \left\{ 1 - \sqrt{1 - \left(\frac{r_{\text{ph}}}{r}\right)^2} \right\}$$

is the dilution factor (Mihalas 1978), and r_{ph} is the photospheric radius.

Lines are treated in the Sobolev approximation. The Sobolev optical depth, τ_{sob} , is a local quantity, given by

$$\tau_{\text{sob}} = \left(\frac{\pi e^2}{m_e c} \right) f_0 n_l \left(1 - \frac{g_l n_u}{g_u n_l} \right) \lambda_0 \frac{dv}{dr},$$

where l designates the lower level of the transition, u the upper level, f_0 is the oscillator strength of the line, n_l and n_u are the occupation numbers of the levels and g_l and g_u are the statistical weights of the levels (Jeffery & Branch 1990).

In SYNOW, a reference line is chosen for each ion and n_l is assumed to vary as e^{-v/v_e} . Thus, τ for the reference line is given as $\tau(v) = \tau e^{-v/v_e}$, where τ is the value of the Sobolev optical depth where the ion begins, usually at the photosphere, v_{ph} , but the line may be detached and begin at a velocity v_{min_e} . Everything else about the ion is assumed to be given by the Boltzmann formulae with a ion temperature T_{exe} . For more information about the SYNOW code see Jeffery & Branch (1990) and Branch et al. (2004; 2005; 2007). The spectral epochs range from almost two weeks pre-maximum to nearly three months post-maximum with wavelengths from roughly 3500 Å to 9500 Å. We take the time of maximum to be February 1, 2014 (Galbany et al. 2015). The spectra are corrected to account for being heavily reddened by dust in the host galaxy as well as for foreground extinction. We use the reddening values found by Goobar et al. (2014).

A good introduction to the analysis of supernova spectra is given in Parrent, Friesen & Parthasarathy (2014, and references therein).

2 PRE-MAXIMUM SPECTRA

Observational details of all of the data used for this work can be found in Paper I. Our earliest observed spectrum was obtained on January 23 (Day -9.6), and we examine a total of 6 spectra obtained between January 23 (Day -9.6) and January 28 (Day -4.6). The pre-maximum spectra all show standard SNe Ia features: Si II $\lambda 6355$, Si II $\lambda 5972$ S II absorption centered at 5300 Å, Mg II absorption centered at 4400 Å as well as 7600 Å $\lambda \lambda 7889.9$, Mg I $\lambda \lambda 5178.3$, and Ca II H+K (absorption centered around 3700 Å) and the IR triplet with absorption centered at 8200 Å. In this time period there is only minimal evolution. The SYNOW spectra include lines of 6 ions: Mg I, Mg II, Si II, S II, Ca II, Fe II. In addition to the photospheric component, Ca II has a detached high-velocity component, and a detachment velocity of $v_{\text{min}_e} = 23,000 \text{ km s}^{-1}$ is used for all of the pre-maximum spectra fits. Values of $v_{\text{phot}} = 14,000 \text{ km s}^{-1}$, and $T_{\text{exe}} = 10,000 \text{ K}$ are used for all ions. A complete list of input parameters can be found in Table 1.

The upper panel of Figure 1 shows the observed spectrum obtained on January 24 (Day -8.5) compared with the SYNOW fit. Here high velocity Ca is fit with a detached high-velocity component. A value of $v_{\text{phot}} = 14,000 \text{ km s}^{-1}$ is used.

The middle panel of Figure 1 shows the observed spectrum obtained on January 28 (Day -4.6) and the SYNOW fit, and the lower panel shows the flattened spectra, where the spectra have been normalized by the local (pseudo) continuum in that wavelength region using the prescription of Jeffery et al. (2007). The Ca II detached high-velocity component persists through this epoch.

The photospheric velocity remains constant throughout this period, the Mg II lines strength is constant, Si II strengthens, S II strengthens, photospheric Ca II lines get stronger, but the high velocity feature remains constant.

Interestingly, we do not find strong spectroscopic evidence for O I $\lambda 7774$, whereas abundance tomography finds that the high velocity ejecta is dominated by oxygen (Ashall et al. 2014). We will discuss this discrepancy in more detail in § 6.

3 NEAR-MAXIMUM SPECTRA

Maximum light occurred on February 1, 2014, and we examine six spectra obtained between February 4 (Day +2.3) and February 14 (Day +12.4). The line identifications remain the same as in § 2 with the addition of Na I D (with absorption centered at 5700 Å), we regard this identification as tentative and note that the presence of both narrow Na II from the ISM of the host and diffuse interstellar bands (Ritchey et al. 2015; Welty et al. 2014) fall in roughly the right wavelength range to match the observed feature. The S II absorption feature declines steadily with time. SYNOW spectra include lines of the following ions: Na I, Mg I, Mg II, Si II, Si III, S II, Ca II, Fe II. The detached high-velocity Ca II component is no longer present, and the Fe II ions are only used for the February 12 (Day +10.5) spectrum. Cu II fits a bump at 5300 Å that is not clearly real due to the dichroic break and we therefore do not identify the line. Since the Fe II appears only in the Day +10.5 its identification is weak. The Na I line is likely, but the large τ found for

Pre-Maximum SYNOW Parameters

Date	v_{phot}	T_{bb}	T_{exe}	Mg I		Mg II		Si II		S II		Ca II		HV Ca II			Fe II	
				τ	v_e	τ	v_e	τ	v_e	τ	v_e	τ	v_e	τ	v_e	v_{min_e}	τ	v_e
Jan 23(-9.6)	14	14	10	1	2	3	2	2	3	1.3	2	15	3	10	3	23	0.5	2
Jan 24(-8.5)	14	14	10	1	2	3	2	2	3	1.3	2	15	3	10	3	23	0.5	2
Jan 25(-7.4)	14	17	10	0.8	2	2	2	3	2	1	2	20	3	10	3	23	0.5	2
Jan 26(-6.5)	14	18	10	1	2	2	2	3	2	1	2	25	3	10	3	23	0.5	2
Jan 27(-5.4)	14	22	10	1	2	2	2	4	2	1.2	2	25	3	10	3	23	0.5	2
Jan 28(-4.6)	14	24	10	1	2	2	2	4	2	1.7	2	35	3	20	3	23	0.5	2

Table 1. SYNOW parameters for Pre-Maximum spectra fits.

the February 6 (Day +4.2) spectrum is due to the dichroic break in the observed spectrum. Values of $v_{\text{phot}} = 12,000$ km s⁻¹, and $T_e = 10,000$ K are used for all ions except for the February 14 (Day +12.4) spectra, in which a value of $v_{\text{phot}} = 11,000$ km s⁻¹ is used. A complete list of input parameters can be found below in Table 2. Comparing with Ashall et al. (2014) our results are somewhat different, by this time they find a significant amount of Fe II, which they take as evidence for ⁵⁶Ni above the photosphere, we do not find strong evidence for this. Na D are typically identified on core normal (or close to core normal) SNe Ia about one week post maximum light (Branch et al. 2008).

The upper left panel of Figure 2 shows the observed spectrum obtained on February 4 (Day +2.3) and the SYNOW fit. The blue and red arms of the observed spectrum were matched at 6000 Å. A value of $v_{\text{phot}} = 12,000$ km s⁻¹ is used. The upper right panel shows the observed spectrum obtained on February 5 (Day +3.3) and the SYNOW fit. Si III is now used in the fit, to help with the absorption produced by the Si III $\lambda\lambda 4425.3$ line and the absorption in the Na I D trough produced by the Si III $\lambda\lambda 5707.5$ line. Since it is only used to help with absorption in blended features, the Si III identification is tentative.

The lower left panel of Figure 2 shows the observed spectrum obtained on February 12 (Day +10.5) and the SYNOW fit. It exhibits Mg I absorption centered at 5000 Å, Mg II absorption centered at 7600 Å and 8900 Å. The Fe II lines are probably a synthetic fluke. A value of $v_{\text{phot}} = 12,000$ km s⁻¹ is used.

The lower right panel shows the observed spectrum obtained on February 14 (Day +12.4) and the SYNOW fit. This is nearly identical to the Day +10.5 fit, but with Si III, weaker Si II, and no Fe II, showing that the Fe II identification in the February 12 (Day +10.5) fit is unlikely. The identification of Si III at this epoch is interesting, since Si III is usually only seen at pre-maximum.

Looking at the four panels in Figure 2, it appears as if the fit to the Mg I doublet degrades with epoch from February 4 to 12, however, in reality the two features seen in absorption at 4750 Å and 5000 Å are stronger in the last epoch and thus, the Mg I identification is provisional.

4 POST-MAXIMUM SPECTRA

Six spectra were obtained between February 19 (Day +17.4) and February 26 (Day +24.5). The post-maximum spectra share the same general features — Si II absorption centered

at 6100 Å, Mg II absorption centered at 7600 Å, Ca II absorption centered at 8200 Å, Fe II absorption centered at 8900 Å, and Na I and Si III absorption centered at 5600 Å, with some variation. Since the Si III is there just to help in the Na I D trough, and it is physically unlikely to have such highly excited ions at this stage, we regard the Si III as weak at this epoch. The SYNOW spectra include lines of 8 ions: Na I, Mg I, Mg II, Si II, Si III, S II, Ca II, Fe II. Values of $v_{\text{phot}} = 11,000$ km s⁻¹ and $T_e = 10,000$ K are used for all ions except for the February 24 (Day +22.5) and February 26 (Day +24.5) spectra, where v_{phot} is reduced to 10,000 km s⁻¹. Table 3 lists the input parameters.

The upper left panel of Figure 3 shows the observed spectrum obtained on February 19 (Day +17.4) and the SYNOW fit, and the upper right panel shows the flattened spectra. The synthetic spectrum is a decent fit. It has several prominent features: Si II absorption centered at 6100 Å, Na I absorption centered at 5700 Å, Mg I absorption centered at 5000 Å, Mg II absorption centered at 7600 Å and 8900 Å, and Ca II absorption centered at 8200 Å. A value of $v_{\text{phot}} = 11,000$ km s⁻¹ is used.

The lower left panel of Figure 3 shows the observed spectrum obtained on February 21 (Day +19.5) and the SYNOW fit. This epoch marks the beginning of the Fe II presence that characterizes the later synthetic spectra with a value of $\tau = 3.0$ and the continued presence of the blackbody bump around 7000 Å. A value of $v_{\text{phot}} = 11,000$ km s⁻¹ is used.

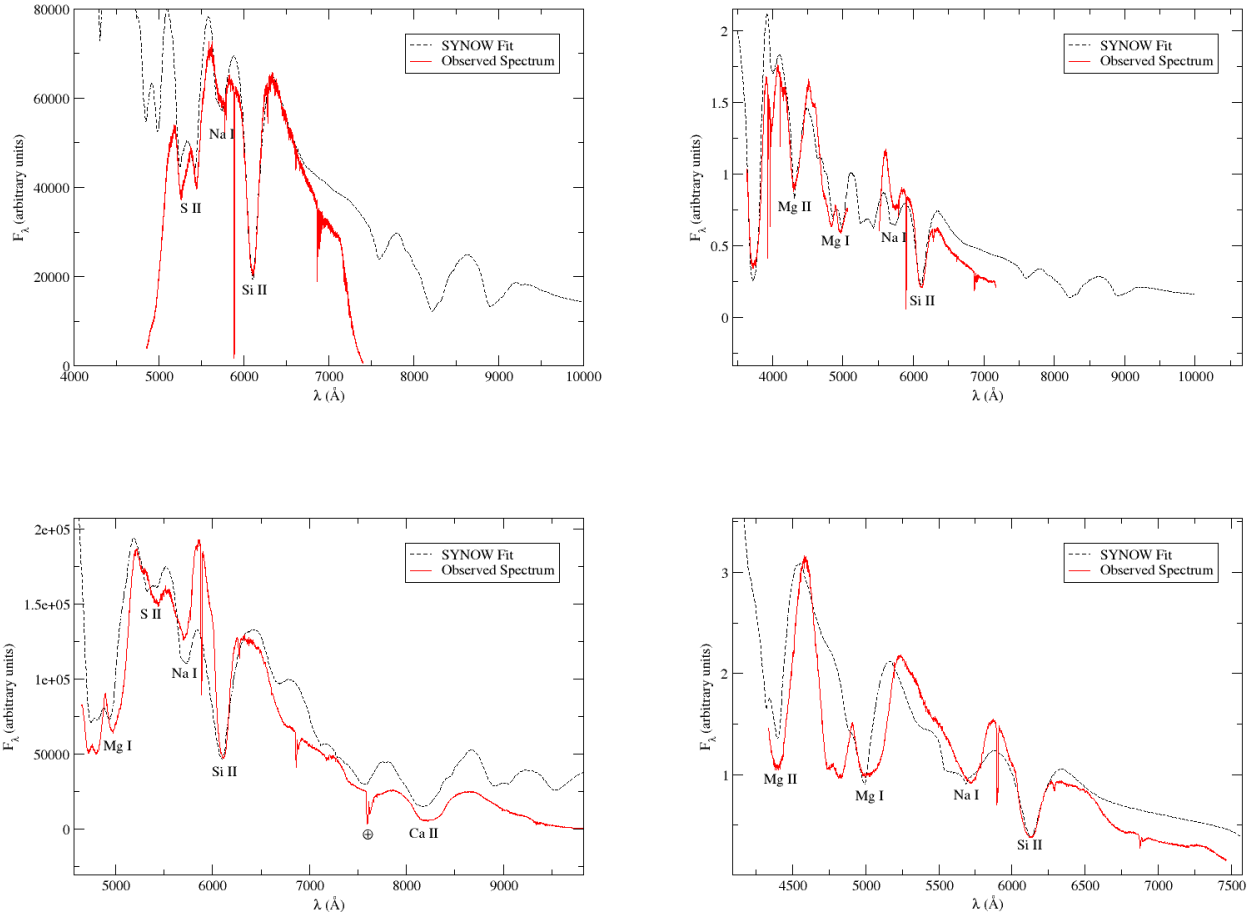
The lower right panel shows the observed spectrum obtained on February 24 (Day +22.5) and the SYNOW fit. As is characteristic of the Post-Maximum Spectra, the synthetic spectrum is a decent fit. Fe II is growing in strength to $\tau = 6.0$. A value of $v_{\text{phot}} = 10,000$ km s⁻¹ is used.

5 LATE SPECTRA

The final spectrum we examined was obtained on May 11 (Day +99.1), and we have 8 spectra obtained between March 6 (Day +33.4) and May 11 (Day +99.1). The late spectra share some general features — Na I absorption centered at 5600 Å, Mg II absorption centered at 7600 Å, Ca II absorption centered at 8200 Å, Co II absorption centered at 5000 Å and 6400 Å, and Fe II absorption centered at 8900 Å — although with far more variation than observed in the earlier epochs. Their SYNOW spectra include lines of 8 ions: Na I, Mg I, Mg II, Ca II, Fe II, Co II, Ni II, and Cu II. The v_{phot} values used decrease from 9,000 km s⁻¹ to 6,000

Near-Maximum SYNOW Parameters

Date	v_{phot}	T_{bb}	T_{exe}	Na I		Mg I		Mg II		Si II		Si III		S II		Ca II		Fe II	
				τ	v_e	τ	v_e	τ	v_e	τ	v_e	τ	v_e	τ	v_e	τ	v_e	τ	v_e
Feb 04(+2.3)	12	11	10	1	2	2	2	2	2	6	2	1	1	2.2	2	30	3	0	2
Feb 05(+3.3)	12	11	10	1	2	2	2	2	2	6	2	1	1	1.2	2	30	3	0	2
Feb 06(+4.2)	12	11	10	10	2	5	2	2	2	6	2	1	1	1.2	2	10	3	0	2
Feb 12(+10.5)	12	11	10	1	2	6	2	0	2	6	2	0	1	0.3	2	180	3	4	2
Feb 14(+12.4)	11	22	10	1	2	3	2	2	2	4	2	10	1	0	2	60	3	0	2

Table 2. SYNOW Parameters for Near-Maximum spectra fits.**Figure 2.** The observed spectra and SYNOW fits representative of the near-maximum epoch. The upper left panel shows the February 4 (Day +2.3) spectra, the upper right panel shows the February 5 (Day +3.3) spectra, the lower left panel shows the February 12 (Day +10.5) spectra, and the lower right panel shows the February 14 (Day +12.4) spectra.

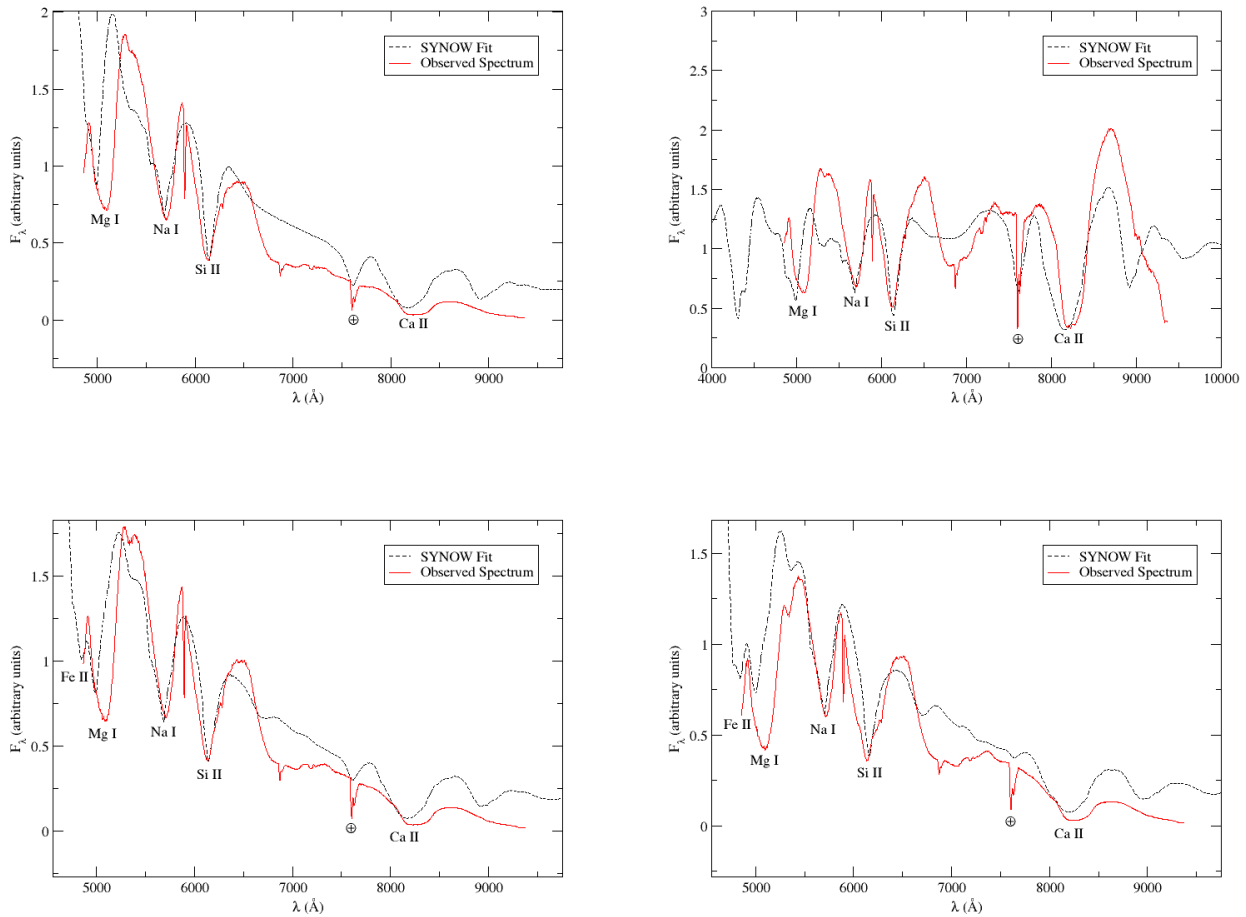
km s⁻¹ as the spectra age, and $T_{\text{exe}} = 6,000$ K is used for the four latest spectra. A complete list of input parameters can be found below in Table 4. The Cu II lines are likely just fitting parameters in that they help fit the iron group element blends around 6400 Å and we do not confidently identify those lines in the observed spectra.

These late times are not strictly in keeping with the Schuster-Schwarzschild approximation of SYNOW. However, because past Day +100 permitted lines dominate the

spectra of SNe Ia (Branch et al. 2008; Friesen et al. 2014), the SYNOW-like assumptions are not invalid at these epochs, although we do make allowance for the variation of the “photosphere” with wavelength at these late times. We note that SYNOW-like assumptions lead to qualitative insights even at very late times (Friesen et al. 2012). This fact allows us to go much further in our analysis than other work that invokes the Schuster-Schwarzschild approximation (Ashall et al. 2014).

Post-Maximum SYNOW Parameters

Date	v_{phot}	T_{bb}	T_{exe}	Na I		Mg I		Mg II		Si II		Si III		S II		Ca II		Fe II	
				τ	v_e	τ	v_e	τ	v_e	τ	v_e	τ	v_e	τ	v_e	τ	v_e	τ	v_e
Feb 19(+17.4)	11	22	10	2.5	2	3	2	6	2	12	1	10	1	0.3	2	200	3	0	2
Feb 20(+18.3)	11	22	10	2.5	2	3	2	4	2	10	1	10	1	0.3	2	180	3	0	2
Feb 21(+19.5)	11	22	10	2.5	2	3	2	3	2	10	1	10	1	0	2	180	3	3	2
Feb 24(+22.5)	10	22	10	2.5	2	3	2	1	2	10	1	10	1	0	2	140	3	6	2
Feb 26(+24.5)	10	22	10	2	2	3	2	2	2	12	1	14	1	0	2	140	3	6	2

Table 3. SYNOW Parameters for Post-Maximum spectra.

Figure 3. The observed spectra and SYNOW fits representative of the post-maximum epoch. The upper left panel shows the February 19 (Day +17.4) spectra, the upper right panel shows the flattened February 19 (Day +17.4) spectra, the lower left panel shows the February 21 (Day +19.5) spectra, and the lower right panel shows the February 24 (Day +22.5) spectra.

The upper left panel of Figure 4 shows the observed spectrum obtained on March 6 (Day +33.4) and the SYNOW fit. The SYNOW fit is now strongly affected by the underlying blackbody and lack of continuum transfer. It has several prominent features — Na I D absorption centered at 5700 Å, Mg I absorption centered at 5000 Å, Mg II absorption centered at 7600 Å and 8900 Å, Fe II and Co II absorption centered at 5000 Å and 6400 Å, and Ca II absorption centered at 8200 Å. The SYNOW spectrum in-

cludes lines of 6 ions: Na I, Mg I, Mg II, Ca II, Fe II, Co II. A value of $v_{\text{phot}} = 9,000 \text{ km s}^{-1}$ is used. A complete list of input parameters can be found in Table 4.

The upper right panel of Figure 4 shows the observed spectrum obtained on March 17 (Day +44.4) and the SYNOW fit. It has several prominent features — Na I absorption centered at 5700 Å, Mg II absorption centered at 7600 Å and 8900 Å, Fe II and Co II absorption centered at 5000 Å and 6400 Å, and Ca II absorption centered at 8200

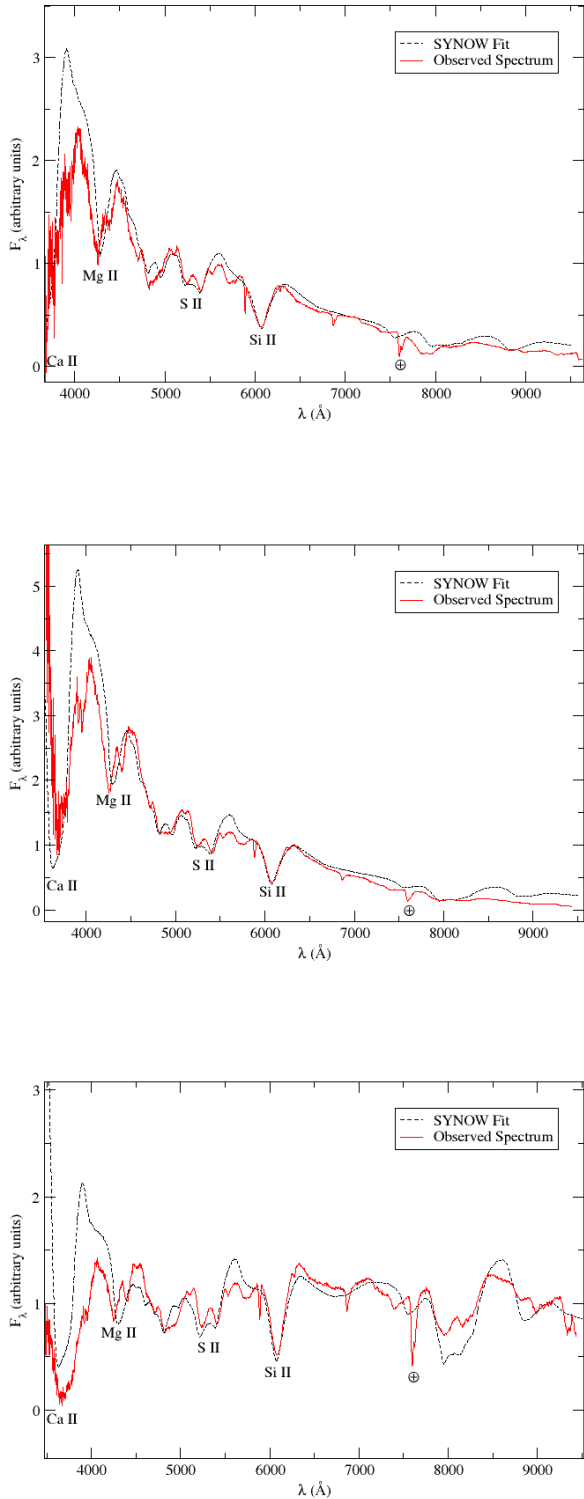


Figure 1. The observed spectra and SYNOW fits representative of the pre-maximum epoch. The upper panel shows the January 24 (Day -8.5) spectra, the middle panel shows the January 28 (Day -4.6) spectra, and the bottom panel shows the flattened January 28 (Day -4.6) spectra.

Å. The SYNOW spectrum includes lines of 6 ions: Na I, Mg II, Ca II, Fe II, Co II, Ni II.

The lower left and lower right panels of Figure 4 show the observed spectrum obtained on May 8 (Day +96.2) and the SYNOW fit over two wavelength regimes. Note that the two figures are split at 8000 Å. For the right figure a much slower v_{phot} of 2,000 km s⁻¹ is used, and $v_e = 4$ is used for Ca II; otherwise it uses the same parameters as that shown on the left. Our use of a blackbody as the inner boundary condition, coupled with the fact that SYNOW does no continuum transfer and is a pure Schuster-Schwarzschild method leads to a bump in the pseudo continuum or line features just to the blue of 7000 Å, this feature becomes even more pronounced at later epochs. The blue fit continues to show Na D absorption centered at 5700 Å, Mg II absorption centered at 7600 Å and 8900 Å, Fe II absorption centered at 5000 Å and 6400 Å, and Ca II absorption centered at 8200 Å. The SYNOW spectrum includes lines of 8 ions: Na I, Mg II, Si III, Ca II, Fe II, Co II, Ni IV. The higher excitation ions (Si III, Ni IV) are weak, but the Ni IV is interesting since that would be evidence of stable nickel and the ionization stage is within the realm of possibility. Values of $v_{\text{phot}} = 9,000$ km s⁻¹ and $T_e = 6,000$ K are used.

These later spectra where we see much deeper into the ejecta are also likely indicating that our exponential density parameterization is too simplistic for the entire ejecta. Our fits are very smooth, whereas the observations show more complex line shapes. The ejecta density profile is more complex, which leads to the observed line shapes, but to introduce more complex density parameterizations is beyond the scope of this work.

6 PHOTOSPHERIC VELOCITY COMPARISONS

Figure 5 shows the photospheric velocities of three supernovae: SN 1994D (Branch et al. 2005), SN 2014J (this work; Paper I; Ashall et al. 2014), and SN 2011fe (Parrent et al. 2012; Mazzali et al. 2014) versus time. The photospheric velocities of SN 2014J and SN 1994D decrease at a similar rate, although SN 2014J maintains a photospheric velocity about 1,000 km s⁻¹ faster than SN 1994D. The photospheric velocity of SN2011fe, on the other hand, decreases at a much faster rate, dropping from 15,000 km s⁻¹ to 8,000 km s⁻¹ in only 14 days. The velocity evolution of abundance tomography of SN 2011fe is similar to that found with SYNOW (Mazzali et al. 2014; Parrent et al. 2012), but the abundance tomography of SN 2014J is somewhat faster than found with SYNOW (Ashall et al. 2014). To a large extent the photospheric velocity and the density slope are degenerate so a shallow density slope can be traded off for a lower photospheric velocity. The slope of the P-Cygni feature from peak to tail can be used to break this degeneracy, but only if one is sure that blending is not important (Baron et al. 1995; Baron, Hauschildt & Mezzacappa 1996).

Figure 5 also shows the velocities of the ions obtained in Paper I (Galbany et al. 2015). The results are in good agreement. Paper I finds high velocity features of Fe II and Ca H+K at early times. Si II $\lambda 6355$, $\lambda 5972$, $\lambda 4130$ match the photosphere well (being a little bit slower than inferred by SYNOW, until the photosphere recedes below the region

Late SYNOW Parameters

Date	v_{phot}	T_{bb}	T_{exe}	Na I		Mg I		Mg II		Ca II		Fe II		Co II		Ni II		Cu II	
				τ	v_e	τ	v_e	τ	v_e	τ	v_e	τ	v_e	τ	v_e	τ	v_e	τ	v_e
Mar 06(+33.4)	9	14	10	2	2	3	2	0	2	0	3	6	2	15	3	10	2	0	2
Mar 07(+34.4)	9	14	10	2	2	3	2	0	2	0	3	6	2	15	3	10	2	0	2
Mar 12(+39.1)	9	8	10	2	2	0	2	0	2	0	3	9	2	15	3	10	2	2	2
Mar 17(+44.4)	9	8	10	3	2	0	2	0	2	0	3	15	2	15	2	10	2	2	2
Apr 08(+66.2)	8	8	06	3	2	0	2	0	2	0	3	60	2	15	2	15	2	4	2
May 08(+96.2)	6	8	06	30	2	40	2	30	2	900	3	50	2	15	2	5	2	5	2
May 09(+97.2)	6	8	06	60	2	0	2	0	2	900	3	40	2	35	2	5	2	8	2
May 11(+99.1)	6	6	06	30	2	5	2	0	2	20	3	15	2	20	2	0	2	8	2

Table 4. SYNOW parameters for Late spectra fits.

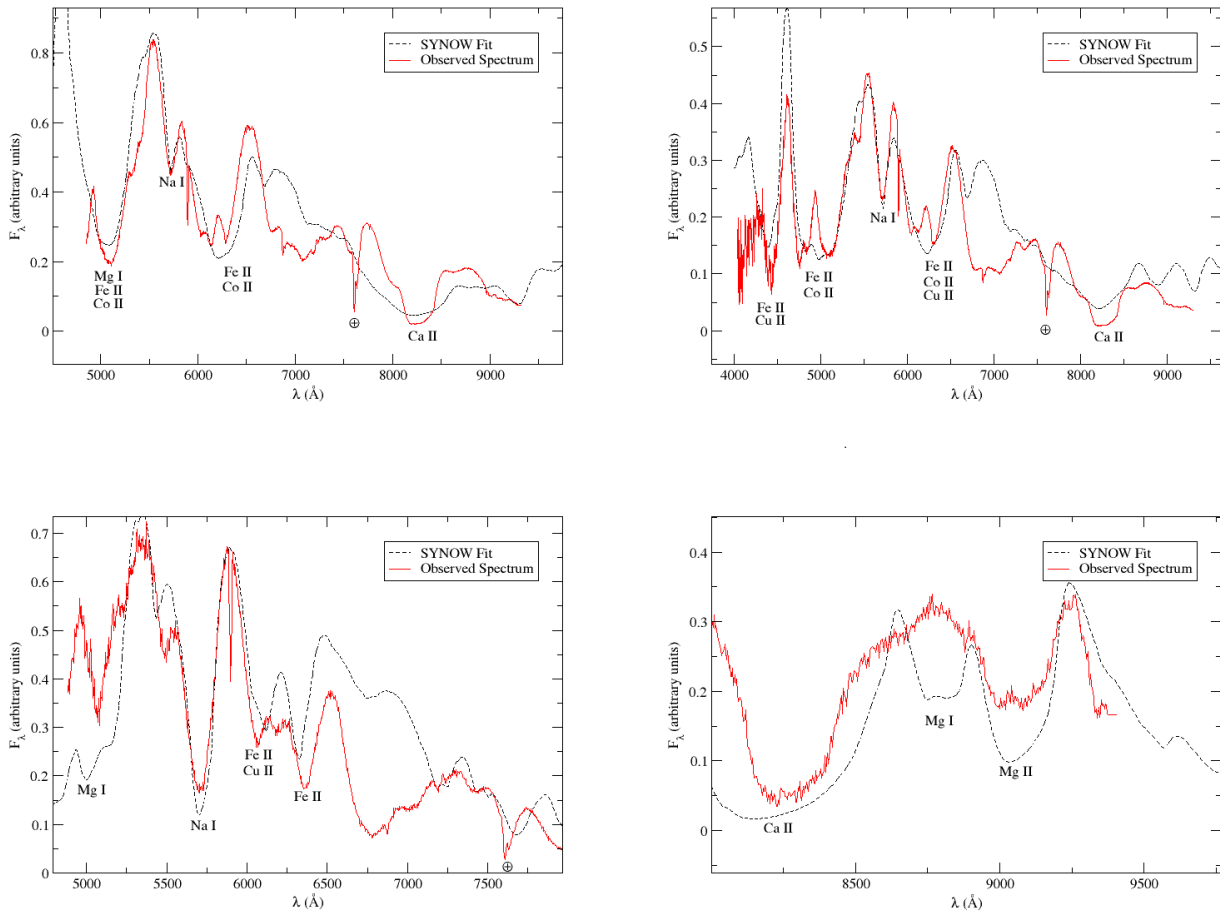


Figure 4. The observed spectra and SYNOW fits representative of the late epoch. The upper left panel shows the March 6 (Day +33.4) spectra, the upper right panel shows the March 17 (Day +44.4) spectra, and the lower left and lower right panels show the May 8 (Day +96.2) spectra, split into two wavelength regimes.

of primary silicon formation. The trend is similar for the S II lines, although they were measured to be marginally slower than the Si II lines. Interestingly, the Mg II lines and the Ca IR triplet lines match the early photosphere very well, until hanging up as the photosphere recedes. At 100 days the Mg II lines are very slow, which is likely simply

due to a mis-identification of the feature. The Fe II lines are the most interesting; they begin with a high velocity component, match well the inferred SYNOW photosphere at about +20 days, fall significantly below the inferred SYNOW photosphere in the +40-50 Day epochs, and then rise again to roughly match the inferred photosphere at Day +100. The

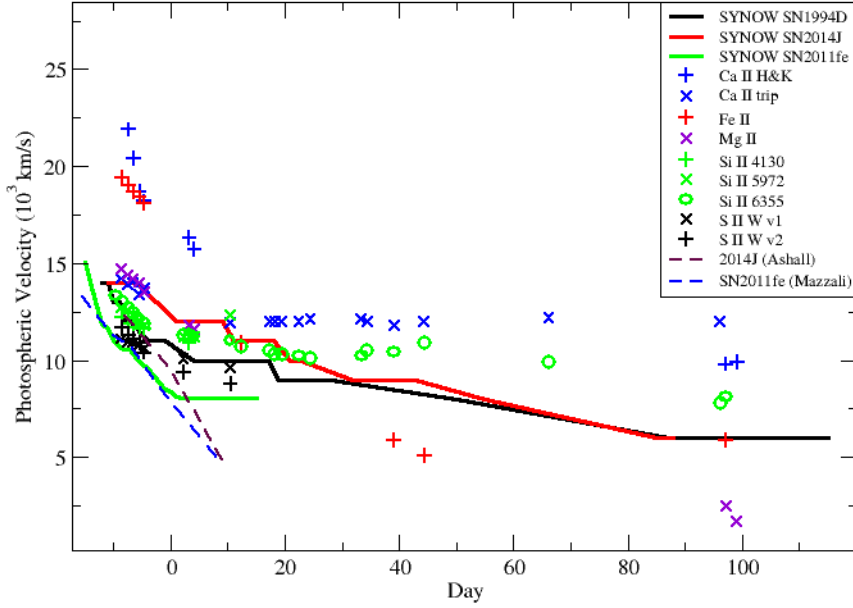


Figure 5. The photospheric velocities of three supernovae: SN 1994D (Branch et al. 2005), SN 2014J (this work, Paper I Ashall et al. 2014), and SN 2011fe (Parrent et al. 2012; Mazzali et al. 2014) versus time. The SYNOW fit velocity for SN 1994D (Branch et al. 2005) is shown in black, the SYNOW fit velocity for SN 2014J (this work) is shown in red, SN 2014J (Ashall et al. 2014) is shown in maroon, the SYNOW fit velocity for SN 2011fe (Parrent et al. 2012) is shown in green, and SN 2011fe (Mazzali et al. 2014) is shown in blue. The points show the observed line velocities taken from Table 2 of Galbany et al. (2015).

variation gives an estimate of the error in inferring ion velocities purely observationally and via a SYNOW approach.

7 COMPARISON WITH SN 2011fe

SN 2011fe is also a nearby and well studied Type Ia supernova. Here, we briefly discuss to what extent a comparison between SNe 2014J and SN 2011fe properties allow us to infer properties about their progenitors and explosion mechanism, although a complete study is beyond the scope of this paper. SN 2014J and SN 2011fe have similar maximum magnitudes, for example, in B SN 2014J: -19.19 ± 0.1 Marion et al. (2015), -19.26 ± 0.1 Kawabata et al. (2014); 2011fe: -19.21 ± 0.1 Richmond & Smith (2012), -19.45 ± 0.08 (Tammann & Reindl 2013), and postmaximum decline rates Δm_{15} , SN 2014J: 1.06 ± 0.06 , averaging the reported values (Tsvetkov et al. 2014; Ashall et al. 2014; Kawabata et al. 2014; Marion et al. 2015); SN 2011fe: 1.11 ± 0.07 (Tammann & Reindl 2013; Richmond & Smith 2012; McClelland et al. 2013; Pereira et al. 2013) and different line and photospheric velocities, up to 1500 km s^{-1} around maximum, as shown in Fig 5. Neither SN 2011fe nor SN 2014J show traces of a single degenerate companion (Lundqvist et al. 2015, but see also Graham et al. 2015) favoring, in principle, the double degenerate scenario. SN 2014J is highly reddened $E(B-V) = 1.2$ (Goobar et al. 2014), while SN 2011fe is not, $E(B-V) = 0.03$ (Mazzali et al. 2014). Observed properties

of both supernovae can be explained by the delayed detonation explosion of a carbon-oxygen white dwarf (WD) with a mass close to the Chandrasekhar mass. In delayed detonation explosion models (Khokhlov 1991; Hoefflich, Khokhlov & Wheeler 1995; Hoefflich & Khokhlov 1996), the main properties for the outcome are (Hoefflich et al. 2010): the composition of the WD — related to the WD progenitors; the central explosion ignition density — related with the accretion rate and/or, in the case of rotation, the time scale of angular momentum loss; and the transition density from deflagration to detonation — the main factor that determines the ^{56}Ni mass, which is a free parameter. To reproduce the light curves, ^{56}Ni masses above $0.51\text{--}0.55$ and $0.6\text{--}0.65 M_{\odot}$ for SNe 2011fe and SN 2014J, respectively, have been estimated (Isern et al. 2013; Baron et al. 2015). Higher transition densities (lower pre-expansions) will produce more ^{56}Ni and less intermediate mass elements, but the corresponding increase in the kinetic energy would be above a factor of 5 smaller than the increase in ^{56}Ni masses. This implies that the differences in the ejecta velocities of SN 2014J with respect to SN 2011fe can not be explained by just increasing the transition density. The observed variation in velocities can possibly, be explained assuming different central ignition densities or different WD chemical compositions, mainly the ratio C/O (Domínguez, Hoefflich & Straniero 2001).

Smaller central ignition densities produce more ^{56}Ni and less neutronized elements in the central regions and, for smaller central densities, the WD binding energy is also

smaller and so, the kinetic energy is higher, while maximum magnitudes and decline rates could be similar for the density range needed to explain these two supernovae. Thus, SN 2014J could have been ignited at a central density smaller than that for SN 2011fe, due to a higher accretion rate or, in case of rotation, to a shorter time scale for the angular momentum losses (Piersanti et al. 2003; Domínguez et al. 2006). If this were the case, the light curve tail of SN 2011fe would be dimmer than that of SN 2014J, as it seems to be in *B* band and less markedly in *V* (Foley et al. 2014), although late observations in the optical of SN 2014J have not yet been published. A greater C/O ratio will produce more ^{56}Ni and more kinetic energy. In fact, an increase of C/O above a 20% will produce an increase above 10% in ^{56}Ni mass, an increase above 1500 km s $^{-1}$ in line velocities and 2000 km s $^{-1}$ in the photospheric velocity (Domínguez, Hoefflich & Straniero 2001). If the difference is due to the differences in the C/O ratio between the progenitors of SN 2014J and SN 2011fe, their light curve tails will be similar — for the range in C/O needed to explain the observed velocities — and SN 2014J will be 0.1 magnitudes brighter at maximum light. Reported observations show that SN 2014J is dimmer at maximum than SN 2011fe, but note that 0.1 mag is within the errors, SN 2014J is heavily reddened and there are discrepancies in the maximum magnitude as derived by different authors. The chemical composition of the exploding WD is related to the properties of the WD progenitors, mainly the initial main sequence mass and, to a smaller extent, the initial metallicity.

Assuming that both WDs are produced in the double degenerate scenario, a decrease of in C/O above 20% are expected just by changing the the initial accreting WD mass from 0.8 to 0.9 M_{\odot} , corresponding to the C+O cores of main sequence masses 5 and 6 M_{\odot} (initial solar composition) and up to 35%, if a 1 M_{\odot} WD (initial main sequence mass 7 M_{\odot}) is considered (Bravo et al. 2010). Smaller differences, in terms of ^{56}Ni masses, would be obtained assuming different WD cooling times, diffusion and crystallization processes, before accretion, for example, an increase of 7% in ^{56}Ni mass increasing the cooling time from 0.6 to 0.8 Gyr, (Bravo et al. 2011) or changing the metallicity (Bravo et al. 2010), i.e. from solar to sub-solar metallicities, as suggested for SN 2011fe (Baron et al. 2015). In both cases, the reason is the central abundance of ^{22}Ne that changes the neutronization and so, the nucleosynthesis (less ^{22}Ne , less neutronization and more ^{56}Ni), but the corresponding changes in kinetic energy/velocities would be smaller than in the previous cases, that is due to varying the C/O ratio or the central density.

In summary, it may be that SN 2014J comes from a smaller primary (and corresponding main sequence) WD mass compared to SN 2011fe, explaining the different observed velocities at maximum, for similar decline rates. In this case similar light curve tail brightnesses would be expected for the range of C/O needed. If the observed maximum magnitude for both SNe were correct and SN 2014J is slightly dimmer at maximum, but showing a brighter light curve tail than SN 2011fe (to be confirmed), it is more likely that SN 2011fe had a greater central ignition density than SN 2014J, this would also explain the smaller expansion velocities of 2011fe. For SN 2011fe a sub-solar metallicity, about $Z_{\odot}/20$, has been suggested (Mazzali et al. 2014; Baron

et al. 2015), this would slightly increase its maximum magnitude.

8 DISCUSSION AND CONCLUSIONS

We do not calculate abundances to compare with Ashall et al. (2014), since in SYNOW the excitation temperature is just a fitting parameter. However, we can compare our results to theirs, and there are some differences. While the early spectra show clear evidence for standard SNe Ia features, we do not find carbon in the spectra, nor do we find oxygen. We also do not find any strong evidence for mixing of nickel to high velocities. We find weak evidence for Si III post maximum (up to Day 23) and Ashall et al. (2014) find no evidence for Si III after Day -7 (Jan 27). The evidence for Si III is not very strong, though, so this difference is not significant. Our results are in basic agreement with the results from INTEGRAL (Churazov et al. 2014, 2015; Diehl et al. 2014, 2015) although due to the low signal to noise there is some ambiguity about just how to interpret the results, that is whether the γ -rays favor symmetric nickel distributions (Churazov et al. 2014, 2015) or asymmetric ones (Diehl et al. 2014, 2015). The mid-IR results seem to indicate a layered, roughly spherically symmetric abundance pattern Telesco et al. (2015).

While abundance tomography (Ashall et al. 2014) indicates the presence of significant oxygen, we do not find any spectroscopic signatures for oxygen at early times and can only weakly identify it at late times. Mg II fits the P-Cygni profile around 4350 Å in the early and the near-maximum spectra, while O I does not. While Mg II doesn't have the same strong identifying feature at 4350 Å in the post-maximum spectra, it does fit the 7600 feature decently well, while adding O I causes an absorption a hundred or so angstroms too blue unless O I is constrained to be within 1,000 km s $^{-1}$ of the photospheric velocity. This is illustrated in Figure 6. It seems odd that O I would be confined to a region so close to the photosphere even though the photosphere has moved from 14,000 km s $^{-1}$ to 6,000 km s $^{-1}$.

There is some reason to doubt the Mg II identification, though, as post maximum spectra do not show a strong feature at Mg II $\lambda\lambda 9226$, and the O I fits do seem to fit the absorption at 9100 Å somewhat. As such, and considering SYNOW's limited applicability at late times, we can't confidently rule out the presence of oxygen at late times. Also, the O I identification is a bit suspect since the O I 7774 line is fit well by the constrained ion, the 9100 Å feature is perhaps better fit by the unconstrained ion. Thus, we should be careful about drawing conclusions about mixing of unprocessed or only slightly processed elements to low velocities.

Just because there is little spectroscopic evidence for oxygen does not mean that it is not there. Since O I has an ionization potential for 16.3 eV, it requires higher temperatures to populate the excited states and so at low temperatures oxygen can be spectroscopically hidden. However, we also do not find any evidence for mixing of ^{56}Ni to high velocities. One would expect that if radioactive ^{56}Ni is mixed to high velocities, then non thermal excitation of oxygen from fast electrons created by γ -ray interactions should be available to excite and ionize significant amounts of oxygen.

Within the limits of our analysis we show that there is

not significant oxygen in the observed spectra and that there appears to be no need for significant mixing of ^{56}Ni into the outer layers of SN 2014J. We find good agreement with the photospheric velocity from other groups using a similar approach, particularly with Paper I. The fast decline found in the photospheric velocity by Ashall et al. (2014) is likely due to a difference in definition, due to their Monte-Carlo approach rather than some important systematic difference in the methods, but the difference in definition is important to keep in mind when comparing velocities determined by different methods.

The late time spectra shown in Figure 4 are in good general agreement with the more detailed modeling results in the IR (Friesen et al. 2014) and in the Mid-IR (Telesco et al. 2015). In general we find features dominated by iron group elements, with features from intermediate group elements such as Ca II and Mg II whose lines become strong at low temperatures. That is, we find evidence for a layered structure that is generically predicted by delayed detonation and pulsating delayed detonation models.

ACKNOWLEDGMENTS

Based on service observations (program SW2014a08) made with the William Herschel Telescope (WHT), and on discretionary observations made with the Isaac Newton Telescope (INT), both operated on the island of La Palma by the Isaac Newton Group (ING) in the Spanish Observatorio del Roque de los Muchachos of the Instituto de Astrofísica de Canarias. We thank the ING Director for having made public the INT data as soon as they were obtained. We also acknowledge the observers who kindly donated their time to monitor SN2014J on both the WHT and the INT. The work has been supported in part by support for program HST-GO-12948.004-A provided by NASA through a grant from the Space Telescope Science Institute, which is operated by the Association of Universities for Research in Astronomy, Incorporated, under NASA contract NAS5-26555. EB acknowledges support from a Carl Bush Fellowship from the University of Oklahoma. Support for LG is provided by the Ministry of Economy, Development, and Tourism's Millennium Science Initiative through grant IC120009, awarded to The Millennium Institute of Astrophysics, MAS. LG acknowledges support by CONICYT through FONDECYT grant 3140566. JIGH acknowledges financial support from the Spanish Ministry of Economy and Competitiveness (MINECO) under the 2011 Severo Ochoa program MINECO SEV-2011-0187, and the 2013 Ramón y Cajal program MINECO RYC-2013-14875, and the Spanish ministry project MINECO AYA2014-56359-P. ID acknowledges MINECO-FEDER grant AYA2011-22460.

REFERENCES

- Amanullah R. et al., 2014, *ApJ*, 788, L21
 Ashall C., Mazzali P., Bersier D., Hachinger S., Phillips M., Percival S., James P., Maguire K., 2014, *MNRAS*, 445, 4427
 Baron E. et al., 2015, *MNRAS*, 454, 2549
 Baron E. et al., 1995, *ApJ*, 441, 170

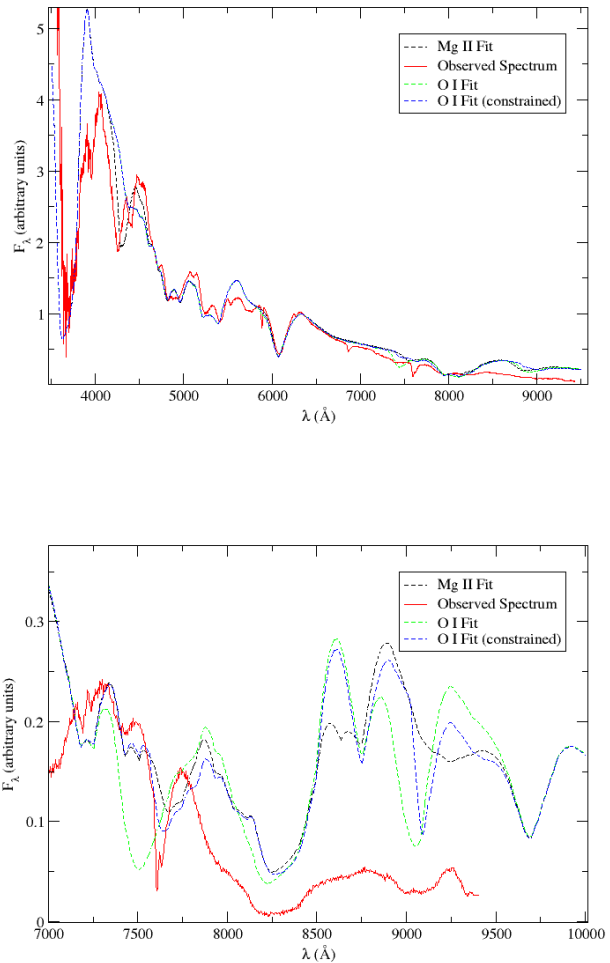


Figure 6. Comparison between Mg II and O I in the synthetic spectra. The upper panel shows an early spectrum (Day -4.6), which emphasizes the need for Mg II to fit the absorption feature near 4300 Å. The lower panel shows a late spectrum (Day +96.2). While Mg II fits the 7600 feature decently well, the O I absorption in this region is far too blue unless oxygen is constrained to a maximum velocity a mere 1,000 km/s above the photospheric velocity. It's worth noting, though, that the O I absorption near 9100 Å does seem to fit a feature of the observed spectrum, so we acknowledge the possible presence of oxygen at late times.

- Baron E., Hauschildt P. H., Mezzacappa A., 1996, *MNRAS*, 278, 763
 Branch D., Baron E., Hall N., Melakayil M., Parrent J., 2005, *PASP*, 117, 545
 Branch D. et al., 2008, *PASP*, 120, 135
 Branch D. et al., 2004, *The Astrophysical Journal*, 606, 413
 Branch D., et al., 2007, *PASP*, 119, 709
 Bravo E., Althaus L. G., García-Berro E., Domínguez I., 2011, *A&A*, 526, A26
 Bravo E., Domínguez I., Badenes C., Piersanti L., Straniero O., 2010, *ApJ*, 711, L66
 Churazov E. et al., 2015, *ApJ*, 62
 —, 2014, *Nature*, 512, 406

- Diehl R. et al., 2014, *Science*, 345, 1162
—, 2015, *A&A*, 574, A72
- Domínguez I., Hoefflich P., Straniero O., 2001, *Nuclear Physics A*, 688, 21
- Domínguez I., Piersanti L., Bravo E., Tornambé A., Straniero O., Gagliardi S., 2006, *ApJ*, 644, 21
- Foley R. J. et al., 2014, *MNRAS*, 443, 2887
- Friesen B., Baron E., Branch D., Chen B., Parrent J. T., Thomas R. C., 2012, *ApJS*, 203, 12
- Friesen B., Baron E., Wisniewski J. P., Parrent J. T., Thomas R. C., Miller T. R., Marion G. H., 2014, *ApJ*, 792, 120
- Galbany L., et al., 2015, *MNRAS*, submitted, *astro-ph/1510.06596*, (Paper I)
- Goobar A. et al., 2014, *ApJ*, 784, L12
- Graham M. L. et al., 2015, *ApJ*, submitted, *astro-ph/1412.0653*
- Hoefflich P., Khokhlov A., 1996, *ApJ*, 457, 500
- Hoefflich P., Khokhlov A. M., Wheeler J. C., 1995, *ApJ*, 444, 831
- Hoefflich P. et al., 2010, *ApJ*, 710, 444
- Isern J. et al., 2013, *A&A*, 552, A97
- Jack D., Baron E., Hauschildt P. H., 2015, *MNRAS*, 449, 3581
- Jeffery D., Branch D., 1990, in *Supernovae*, Wheeler J. C., Piran T., eds., World Scientific, Singapore, p. 149
- Jeffery D. J., Ketchum W., Branch D., Baron E., Elmhamdi A., Danziger I. J., 2007, *ApJS*, 171, 493
- Johansson J. et al., 2015, *MNRAS*, submitted, *astro-ph/1411.3332*
- Kawabata K. S. et al., 2014, *ApJ*, 795, L4
- Kelly P. L. et al., 2014, *ApJ*, 790, 3
- Khokhlov A., 1991, *A&A*, 245, 114
- Lundqvist P. et al., 2015, *A&A*, 577, A39
- Margutti R., Parrent J., Kamble A., Soderberg A. M., Foley R. J., Milisavljevic D., Drout M. R., Kirshner R., 2014, *ApJ*, 790, 52
- Marion G. H. et al., 2015, *ApJ*, 798, 39
- Mazzali P. A., et al., 2014, *MNRAS*, 439, 1959
- McClelland C. M., Garnavich P. M., Milne P. A., Shappee B. J., Pogge R. W., 2013, *ApJ*, 767, 119
- Mihalas D., 1978, *Stellar Atmospheres*. W. H. Freeman, New York
- Nielsen M. T. B., Gilfanov M., Bogdán Á., Woods T. E., Nelemans G., 2014, *MNRAS*, 442, 3400
- Parrent J., Friesen B., Parthasarathy M., 2014, *Ap&SS*, 351, 1
- Parrent J. T., et al., 2012, *ApJ*, 752, L26
- Pereira R., et al., 2013, *A&A*, 554, A27
- Pérez-Torres M. A. et al., 2014, *ApJ*, 792, 38
- Piersanti L., Gagliardi S., Iben, Jr. I., Tornambé A., 2003, *ApJ*, 583, 885
- Richmond M. W., Smith H. A., 2012, *Journal of the American Association of Variable Star Observers (JAAVSO)*, 40, 872
- Ritchey A. M., Welty D. E., Dahlstrom J. A., York D. G., 2015, *ApJ*, 799, 197
- Siverd R. J., Goobar A., Stassun K. G., Pepper J., 2015, *ApJ*, 799, 105
- Tammann G. A., Reindl B., 2013, *A&A*, 549, A136
- Telesco C. M. et al., 2015, *ApJ*, 798, 93
- Tsvetkov D. Y., Metlov V. G., Shugarov S. Y., Tarasova T. N., Pavlyuk N. N., 2014, *Contributions of the Astronomical Observatory Skalnaté Pleso*, 44, 67
- Welty D. E., Ritchey A. M., Dahlstrom J. A., York D. G., 2014, *ApJ*, 792, 106